Vokasi Unesa Bulletin of Engineering, Technology and Applied Science (VUBETA)
https://journal.unesa.ac.id/index.php/vubeta
Vol. 3, No. 2, 2026, pp. 269~279 DOI: 10.26740/vubeta.v3i2.46268
ISSN: 3064-0768

Benz Limit Optimal Design for Double Fed Induction Generator and Kundru’s Multimachine integration

Abel E. Airobman[1], Sabo Aliyu[2], Isiaka B. Musa[3*]
[1,2]Department of Electrical and Electronics Engineering, Faculty of Engineering, Post Graduate School, Nigerian Defense Academy, Nigeria
[3]Kaduna Electricity Distribution Company, Kaduna State, Nigeria

Article Info

Article history:

Received October 21, 2026
Revised January 22, 2026
Accepted March 15, 2026

Keywords:

Benz limit
Controllers
Oscillations
Output voltage
Phase angle

ABSTRACT

The study explores the integration of an optimal Benz limit Doubly Fed Induction Generator (DFIG) with IEEE Kundur's test multi-machine power system, emphasizing the use of meta-heuristic algorithms and controllers. This work is scoped at the DFIG power coefficient, output voltage, and phase angle oscillations during integration. The controllers’ performances were compared with three techniques: the hippopotamus (HO), Sine cosine (SC), and Morth flame (MFO) algorithms to verify the competence of the proposed method in achieving better system stability. To improve the proposed Hybrid Multi-source integration of DFIG, Hydrogen Fuel Cell (HFC) to augment (Wind, Solar cell, Battery energy storage system), the proposed work presents the mathematical formulation of DAE, the designed models, and the implementation of wind aerodynamic/mechanical coupling shaft. ODE as solver in MATLAB 2021a Simulink environment as presented. The results presented an optimal Benz limit for the blade tip speed ratio λ_{opt} = 8.1, blade pitch angle β=0, rotor power coefficient C_p= C_{pmax} =0.48, and turbine output power P_t =5 MW described by equation 7. A symmetrical fault was set up on bus 2 at t = 1 second; the governor load reference increased by 1%, the system loading by 1%; and a nonlinear time-domain simulation was carried out on the integrated network to assess controllers’ robustness. Likewise, the result validates the usefulness of the proposed SC, HO, and MFO tuned Tilt, PID for DFIG output voltage and phase angle control that outperforms the traditional MFO tuning techniques in terms of resilience, efficiency, and convergence.

1. INTRODUCTION

Energy sources such as wind, geothermal, solar, biomass, and hydrogen fuel cells have been increasingly integrated into power grid systems to meet energy needs and reduce carbon emissions. These systems are rapidly growing in integration and development [1]. Variable-speed wind turbines are the result of technological developments in wind energy; they can capture the maximum amount of wind energy across a range of wind speeds. DFIG, a well-liked wind energy conversion device, improves power quality (generating and absorbing reactive power) and offers high power output efficiency [2]. Grid stability and overall system performance, however, need to be considered. The regulation and stability of the electrical grid are affected by the distinct power characteristics of wind energy conversion systems based on power electronics converters, as opposed to traditional synchronous generator-based systems [3].

According to Betz, the actual percentage is 59.3%, indicating that only 59.3% of the wind's kinetic energy can be used to turn the turbine and produce power. In reality, turbines cannot reach the Betz limit and usually have an efficiency of 35 to 45 percent. The greatest power it can transform into motion and electricity is known as the Betz limit [4]. The complexity and instability of the system arise from the interconnection of conventional power sources across different areas, leading to mismatches between demand and generation.

*Corresponding Author
Email: isiakamusa905@gmail.com

This results in frequency, tie-line power, and voltage deviations, which affect power quality and reliability [5][6]. Traditional methods of frequency control and voltage regulation are ineffective in solving these problems. This research proposes using the SC, MFO, and HO algorithms to optimize gains of the (PID and Tilt) controllers and minimize error signals to achieve minimum DFIG output voltage and phase angle deviations in an IEEE Kundur's two-area power test system [7].

2. METHOD

A turbine, gearbox, filter, induction generator, and power electronics converters make up DFIG. The DC/AC grid-side converter and the AC/DC rotor-side (machine-side) converter are examples of power electronics converters. The gearbox connects the wind turbine to the induction generator, which uses the turbine's mechanical energy to produce electricity. DFIG provides reactive and active power regulation as well as a variety of variable-speed operations, and is highly appealing for wind energy generation [8]-[9]. Figure 1 depicts the DFIG system.

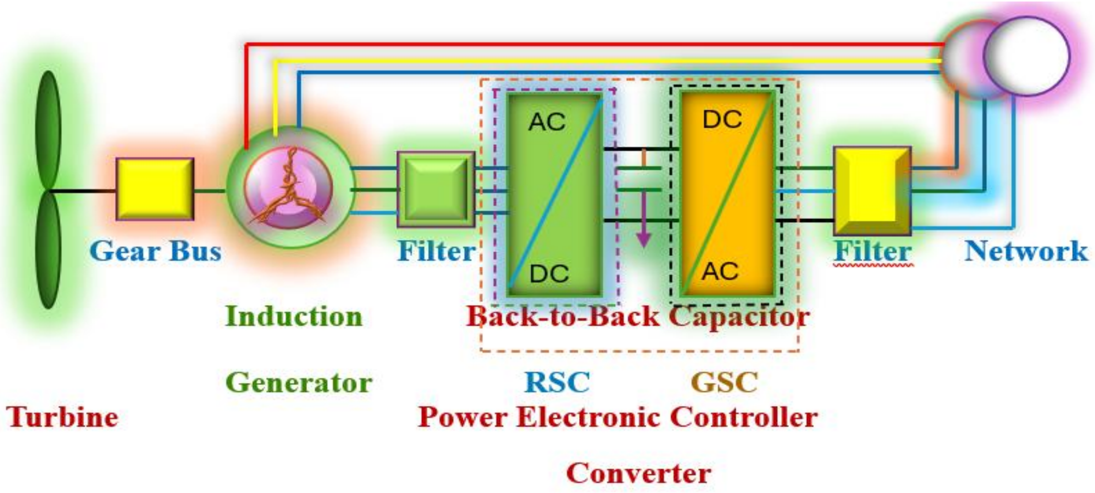

Figure 1. DFIG-WECS system [8]

The aerodynamic mathematical formulation model, the wind turbine's mechanical power (Pm), and the rotational speed V_w are related. The drive train and wind aerodynamic models link the wind speed to the rotor speed of the induction generator. Equation (1) expresses the wind aerodynamic model, which is used to depict the rotor's wind power extraction. It gives the drive train the mechanical power output (Pm), which is dependent on the wind speed (V_w), power coefficient (C_p) and turbine blade length (R) [8].

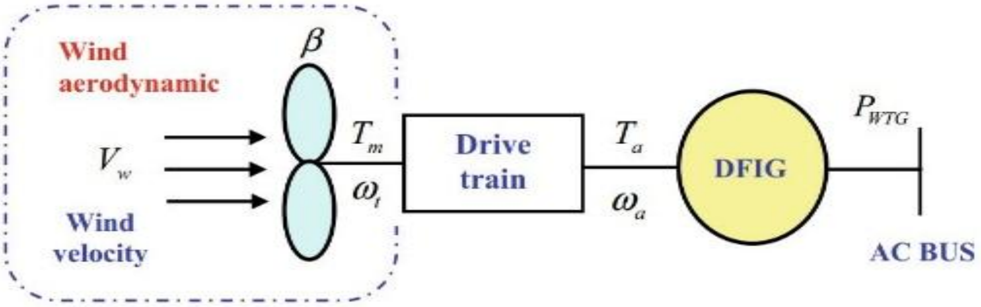

Figure 2. Schematic diagram of wind power system [8]

Wind energy is converted into mechanical energy by wind aerodynamics, and the WPS's electrical power output fluctuates with wind speed and weather. The rotor Cp calculates the amount of energy extracted, and the mechanical power is proportional to the wind speed cube [8].

where $A_{blade}(=\pi R^2)$ is the swept area of the blade in m^2; ρ_{air} is air density in Kg/m3; ωt represents the wind turbine mechanical angular rotor speed in rad/s; R is the radius of the blade in m; $\alpha 1$ to $\alpha 6$ are the coefficients [8]-[9].

$$P_m = \frac{1}{2}\rho_{air}A_{blade}V^3C_p(\lambda,\beta) \tag{1}$$

$$C_p(\lambda,\beta) = (\frac{\alpha_2}{\lambda_i} - \alpha_3\beta - \alpha_4)e^{-\frac{\alpha_5}{\lambda_i}} + \alpha_6\lambda \tag{2}$$

where $\frac{1}{\lambda_i} = \frac{1}{\lambda+0.08\beta} - \frac{0.035}{\beta^3+1}$ (3)

$$\lambda = \frac{\omega_t R}{V_w} \tag{4}$$

$$C_p(\lambda) = \kappa_2\lambda^2 + \kappa_1\lambda + \kappa_0 \tag{5}$$

where κ_2, κ_1 and κ_0 are the constant coefficients. Under the stochastic alteration of wind speed, the maximum power can be derived by setting $\frac{dC_p(\lambda)}{d\lambda}$ =0, i.e.,

$$\frac{dC_p(\lambda)}{d\lambda} = 2k_2\lambda + k_1 = 0 \tag{6}$$

$$\lambda^{opt} = \left(\frac{k_1}{2k_2}\right)$$

where λ^{opt} represents the optimal tip-speed ratio.

$$C_p(\beta,\lambda) = 0.5176\left(\frac{116}{\lambda+0.08\beta} - \frac{4.06}{1+\beta^3} - 0.4\beta - 5\right)e^{\left(\frac{-21}{\lambda+0.08\beta}+\frac{0.735}{1+\beta^3}\right)} + 0.0068\lambda \tag{7}$$

In contrast, the drive train is represented and drives the induction generator using the mechanical output from the wind aerodynamic model.

$$\frac{d\omega_g}{dt} = \frac{1}{2H_g}\left(T_s - T_g\right) \tag{8}$$

$$T_s = K_{tg}\theta_{tg} + C_{tg}\frac{d}{dt}\theta_g \tag{9}$$

$$\frac{d}{dt}\theta_{tg} = \omega elB(\omega_t - \omega_s) \tag{10}$$

$$\frac{d}{dt}\omega_t = \frac{1}{2H_t}(T_t - T_s) \tag{11}$$

where subscripts g, s, and t refer to the generator, shaft, and turbine, respectively. ω represents the rotor speed of the generator, θ_{tg} is the shaft angle twist of the generator, H is the generator inertia, and T represents the drive train shaft stiffness, C_{tg} is the coefficient of damping of the drive train, and ωelb is the electrical base speed.

Induction generator: The generator takes the rotor speed from the turbine and the generator bus voltage from the network model as inputs; in turn, it generates the output current and electrical torque. The name DFIG stands for a device with two feeds: the stationary stator and the rotating rotor. The arrangement of the stator windings creates a magnetic field that rotates the rotor in the air gap at an angular speed due to the output stator currents. Similar to the traditional power grid system, the generator uses the d_q reference frames. These reference frames represent the stator currents.

$$\frac{L'_s}{\omega elB}\frac{d}{dt}i_{sd} = -\omega_s L'_s i_{sq} - R_1 i_{sd} + \frac{e'_{sq}}{\omega_s T_r} + \frac{\omega_g e'_{sd}}{\omega_s} + v_{sd} + K_{mrr}v_{rd} \tag{12}$$

$$\frac{L_s'}{\omega\text{elB}}\frac{d}{dt}i_{sq} = \omega_s L_s' i_{sd} - R_1 i_{sq} - \frac{e_{sd}'}{\omega_s T_r} + \frac{\omega_g e_{sq}'}{\omega_s} - v_{sq} + K_{mrr} v_{rq} \tag{13}$$

The text describes a system with stator currents, electrical base speed, generator and shaft speed, transient stator inductance, stator voltages, rotor voltages, K_{mrr}transformational parameter, and generator voltages behind transient impedances, based on Park's transformation [8][9].

$$\frac{1}{\omega_s \omega elB}\frac{d}{dt}e_{sd}' = -R_2 i_{sq} - \left(1 - \frac{\omega_g}{\omega_s}\right) e_{sq}' - \frac{e_{sd}'}{\omega_s T_r} + K_{mrr} v_{rq} \tag{14}$$

$$\frac{1}{\omega_s \omega elB}\frac{d}{dt}e_{sq}' = -R_2 i_{sd} + \left(1 - \frac{\omega_g}{\omega_s}\right) e_{sd}' - \frac{e_{sd}'}{\omega_s T_r} + K_{mrr} v_{rd} \tag{15}$$

where e_{sq}' and e_{sd}' relate the rotor flux ψ_{rq} and ψ_{rd}, respectively, by Equations (16) and (17):

$$e_{sd}' = -K_{mrr}\omega_s \psi_{rq} \tag{16}$$

$$e_{sq}' = -K_{mrr}\omega_s \psi_{rd} \tag{17}$$

The stator and rotor fluxes themselves are given by Equations:

$$\psi_{rq} = L_r i_{rq} + L_m i_{sq} \tag{18}$$

$$\psi_{rd} = L_r i_{rd} + L_m i_{sd} \tag{19}$$

$$\psi_{sd} = L_s i_{sd} + L_m i_{rd} \tag{20}$$

$$\psi_{sq} = L_s i_{sq} + L_m i_{rq} \tag{21}$$

where L_r, L_m, L_s represent the rotor, mutual, and stator inductances, correspondingly; the rotor generator currents are given by Equations (22) and (23):

$$i_{rq} = \left(\frac{e_{sd}'}{X_m}\right) - K_{mrr} i_{sq} \tag{22}$$

$$i_{rd} = \left(\frac{e_{sq}'}{X_m}\right) - K_{mrr} i_{sd} \tag{23}$$

The equations describe the reactive and active powers of the generator rotor and stator, as well as the electrical torque.

$$P_r = V_{rq} i_{rq} + V_{rd} i_{rd} \tag{24}$$

$$Q_r = -V_{rq} i_{rd} + V_{rd} i_{rq} \tag{25}$$

$$P_s = V_{sq} i_{sq} + V_{sd} i_{sd} \tag{26}$$

$$Q_s = -V_{sq} i_{sd} + V_{sd} i_{sq} \tag{27}$$

The filter connects the rotor windings of the power grid system. This study employed an inductor–capacitor–inductor (LCL) type of filter, which consists of a damping resistor R_c, a capacitor C_f, and two inductors (Li, Lg), Inverter voltage (v_{iq}, v_{id}) and stator voltage (v_{sq}, v_{sd}) are inputs to the LCL model, which outputs the current injected into the grid via the filter (i_{gq}, i_{gd}). The represented currents are those that enter the filter.

$$\frac{L_i}{\omega_b}\frac{d}{dt}ii_q = v_{iq} - v_{cq} - (R_i + R_c) ii_q + \omega_g L_i ii_d + R_c i_{gq} \tag{28}$$

$$\frac{L_i}{\omega_b}\frac{d}{dt}ii_d = v_{id} - v_{cd} - (R_i + R_c) ii_d - \omega_g L_i ii_q + R_c i_{gd} \tag{29}$$

Filter currents exiting are given in Equation (31):

$$\frac{L_i}{\omega_b}\frac{d}{dt}i_{gq} = v_{cq} - v_{sq} - (R_g + R_c)i_{gq} + \omega L_g i_{gd} + R_c ii_q \tag{30}$$

$$\frac{L_i}{\omega_b}\frac{d}{dt}i_{gd} = v_{cd} - v_{sd} - (R_g + R_c)i_{gd} + \omega L_g i_{gq} + R_c ii_d \tag{31}$$

The filter capacitor voltage is represented by (33)

$$\frac{C_f}{\omega_b}\frac{d}{dt}v_{cq} = ii_q - i_{gq} - \omega C_f v_{cd} \tag{32}$$

$$\frac{C_f}{\omega_b}\frac{d}{dt}v_{cd} = ii_d - i_{gd} - \omega C_f v_{cq} \tag{33}$$

Lastly, the reactive and active powers exiting the filter are represented.

$$P_{gsc} = V_{iq}i_{iq} + V_{id}i_{id} \tag{34}$$

$$Q_{gsc} = -V_{sq}i_{gd} + V_{sd}i_{gq} \tag{35}$$

The power electronics converters: The systems developed represent mechanical or electrical subsystems of the DFIG power test system and differ from controllers or converters. Power electronics converters, including machine-side and grid-side converters, have a simple two-cascaded proportional-integral model. The machine-side converter receives voltages, generator rotor speed, and current [13][14]. The block diagram of the machine-side converter is shown in Figure 3.

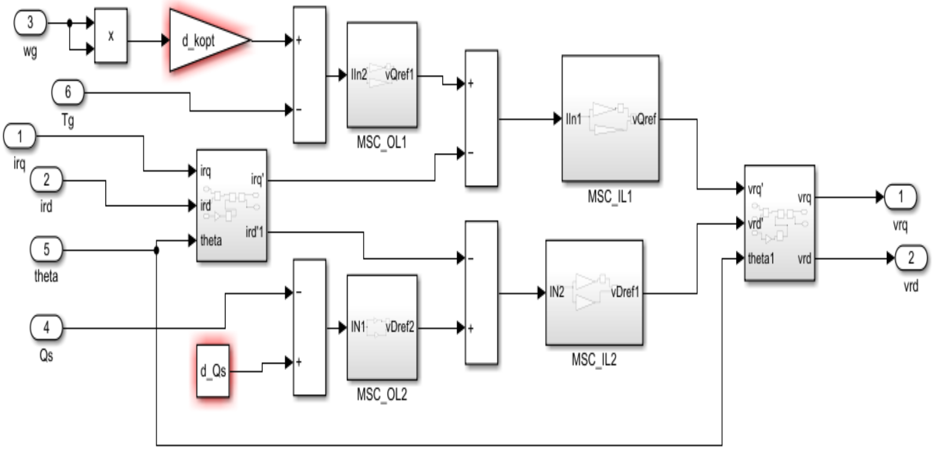

Figure 3. Simulink representation of the machine-side converter [13]

The grid-side controller, like the machine-side converter, uses two cascaded proportional integral controllers to regulate the voltage capacitor and reactive power flow at the wind turbine generator bus [13][14]. The Simulink representation of the grid-side converter is shown below in Figure 4.

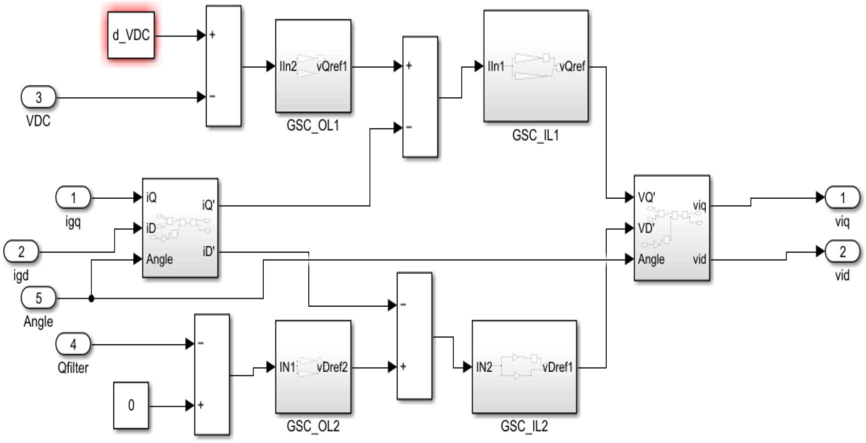

Figure 4. Simulink representation of the grid-side converter [14]

Wind energy torque is transmitted to the generator rotor via a mechanical shaft. Two-mass system (used to amplify the rotor speed at varying wind), which represents WPS shaft dynamics, coupling a low-speed turbine and a high-speed generator through a gearbox, spring, and damper system, as shown in Figure 5. The mechanical coupling shaft's dynamics are described using equation (38), which includes mechanical torque (Tm), generator torque (T_{gen}), inertia constants ((H_r and Hg), rotor damping coefficients (Dr and Dg), internal torque(T_{sr}), and shaft stiffness constant [14].

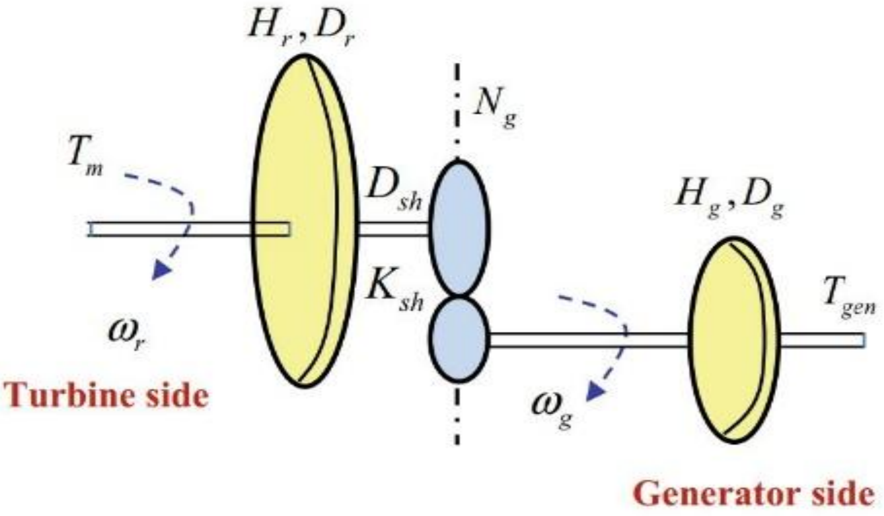

Figure 5. Conceptual mechanical connection shaft two-mass model [14]

$$\frac{d\omega_r}{dt} = \left(-\frac{D_r+D_{sh}}{H_r}\right)\omega_r + \left(\frac{D_{sh}}{H_r}\right)\omega_g - \frac{T_{sr}}{H_r} + \left(\frac{1}{H_r}\right)T_m \tag{36}$$

$$\frac{d\omega_g}{dt} = \left(\frac{D_{sh}}{2H_g}\right)\omega_r - \left(\frac{D_g+D_{sh}}{H_g}\right)\omega_g + \frac{T_{sr}}{N_g H_g} - \left(\frac{1}{H_g}\right)T_{gen} \tag{37}$$

$$\frac{dT_{sr}}{dt} = K_{sh}\left(\omega_r - \frac{\omega_g}{N_g}\right) \tag{38}$$

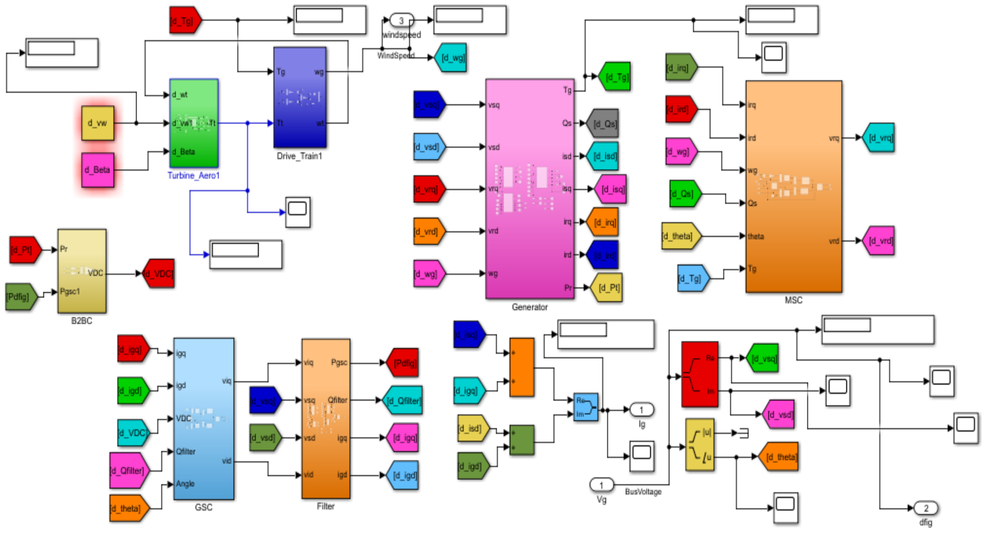

Figure 6. Simulink representation of DFIG [14]

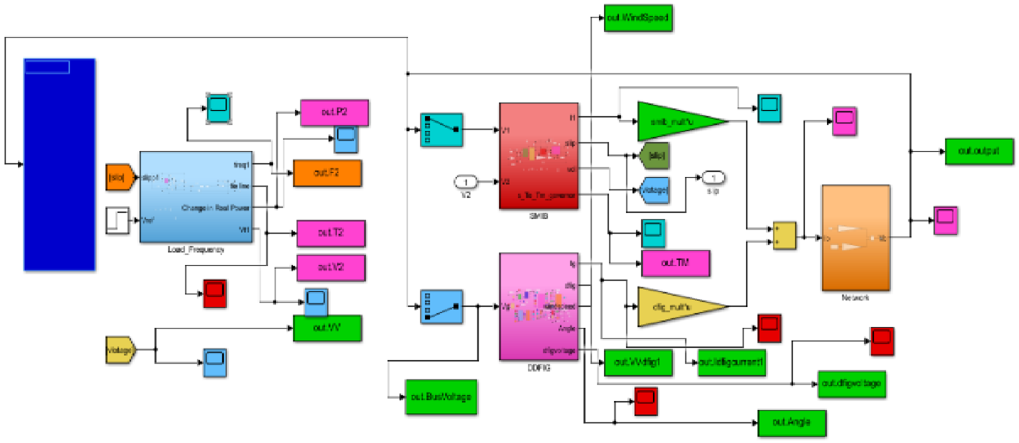

Figure 7. Simulink representation of the SMIB and DFIG system integration [14]

Multimachine Kundur’s two-area Test System: Kundur's two-area test system, an IEEE benchmark power test system, was used in this investigation. It has two synchronous generators in each area, eleven buses, and four (4) synchronous generators. Bus 3, connected to synchronous generator 2, is considered the slack bus.

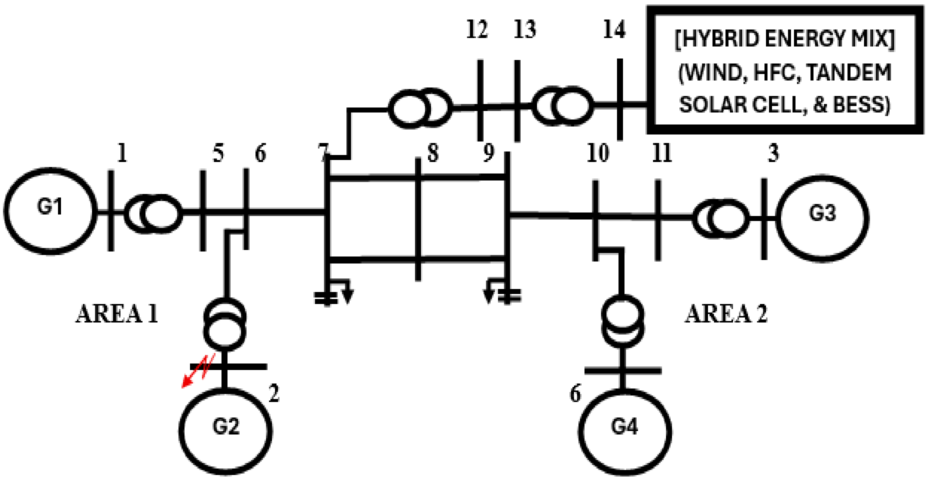

Figure 8. Multi-machine power system Kundur’s two-area test system [14]

A DFIG integrated at bus 14 was added to this power test system in Figure 7 above, converting it to a fourteen (14) bus network. An illustration of the updated power test system on a single line is shown in Figure 8. The bus and line data of the four-machine, Kundur's two-area system in actual values are presented [14].

3. RESULTS AND DISCUSSION

This paper presents simulation results generated from the implementation of the methodology in MATLAB/Simulink. Most importantly, the optimal rotor power coefficient, simulation of HO, SC, and MFO algorithms, and their performance evaluation on the IEEE Kundur test systems. The system was subjected to some operating conditions (perturbations) such as a three-phase fault without a damping controller (i.e., a symmetrical fault was applied to bus 2 at t = 1 second), governor load reference increased by 1% in SMIB, system loading by 1%, and a time-domain simulation that was nonlinear was carried out on the integrated Multimachine network. The SMIB, DFIG, and the integrated electrical or power system structure used were modeled in the SIMULINK environment, and the complete system data are available in [13][14]. Finally, in this paper, we evaluate the performance of the DFIG using power coefficient, phase angle, and output-voltage deviations, and HO, SC, and MFO controllers based on the algorithms.

3.1. Power Coefficient (C_p) Tuning and DFIG Optimal Power Output

Optimization of the power coefficient to obtain an optimal theoretical power output of DFIG. $C_p(\beta, \lambda)$ is the C_p of the blades, which solemnly depend on pitch angle (β) and tip speed ratio (λ). The theoretical maximum value of C_p is limited to 0.593, which is called the **Betz limit**. Table 1 presents the comparison of the simulated power coefficient and the Betz limit.

Table 1. Simulated power coefficient

Betz Limit (Cp)/Simulated result	Pitch Angle (β)	Tip Speed Ratio (λ)
0.593	-	-
0.480	0.0	8.1

The β of the wind turbine data used in this study ranges from 0 to 23 degrees; when the blades are facing the wind and generating the most energy, β is 0 degrees. Figure 9 displays C_p plots for various β values (0, 4, 8, 12, 16, and 24 degrees). As the β is increased to turn the blades away from the wind, it is evident that C_p drops. The λ affects C_p (and consequently, turbine output power P_t) for a given V_w and β. The turbine speed w_t can be adjusted to alter the λ.

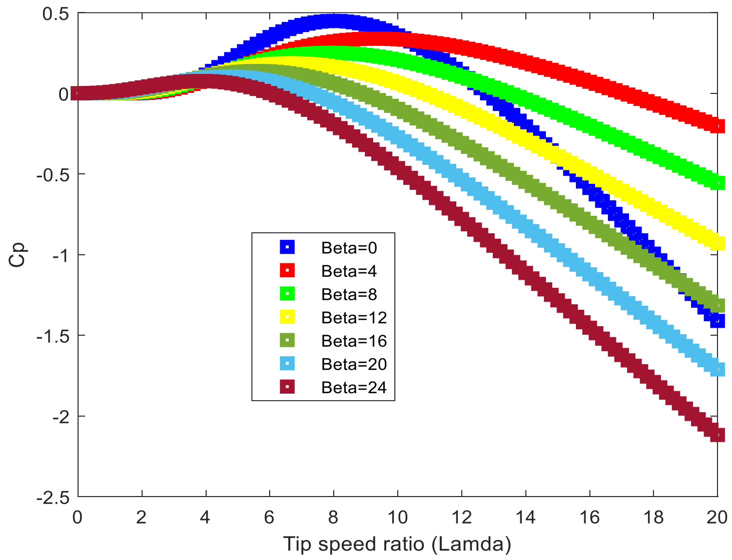

Figure 9. Plot of turbine performance coefficient versus tip speed ratio for different pitch angles.

When the blades are facing the wind, the highest value for C_p is obtained for β=0. Figure 9 shows a solid blue line plotting C_p vs λ Lamda for β=0. For the above turbine settings, the optimal λ value at β = 0 is at λ_{opt}

= 8.1, where the maximum value of C_p, C_{pmax} = 0.48, occurs. Substituting C_p= C_{pmax} and P_t =5 MW in Figure 9, the V_w required to produce the rated output at β=0 is obtained as 15 m/s. This is the rated V_w of the turbine. The rated V_w, above is the β of the turbine is increased to reduce C_p to limit output to 5 MW as presented in equation 7 after substitution of the coefficients.

3.2. Phase Angle Variation Characterization for Algorithm Robustness

Optimization curve for HO, SC, and MFO damping controller, analytical clarification of why HO is superior compared to SC and MFO, presented in Figure 10.

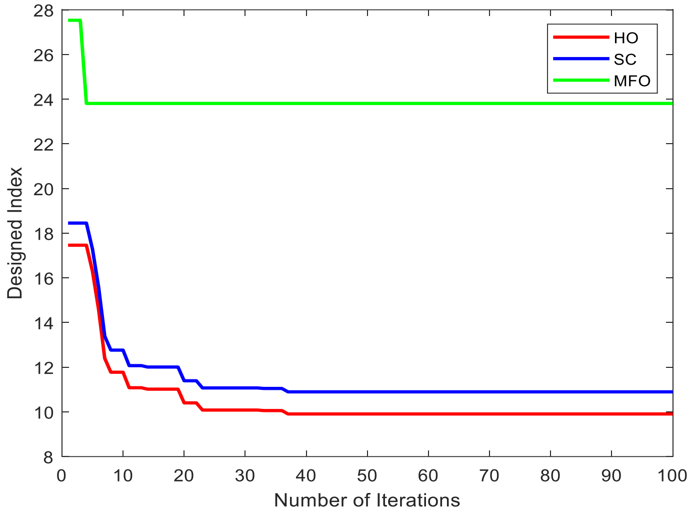

Figure 10. Optimization curve for HO, SC, and MFO damping controller

Figure 11, presented integrated phase angle variation damping and robustness of HO, SC and MFO contorllers based performances, however the operating conditions for controller design robustness (Symmetrical fault was situation on bus 2 at *t* = 1 second, shown in Figure 8, governor load reference increased by 1%, system loading increased by 1%, and a time-domain simulation that was nonlinear was carried out on the integrated Multi-machine IEEE Kundur's test system and DFIG network) were unchanged.

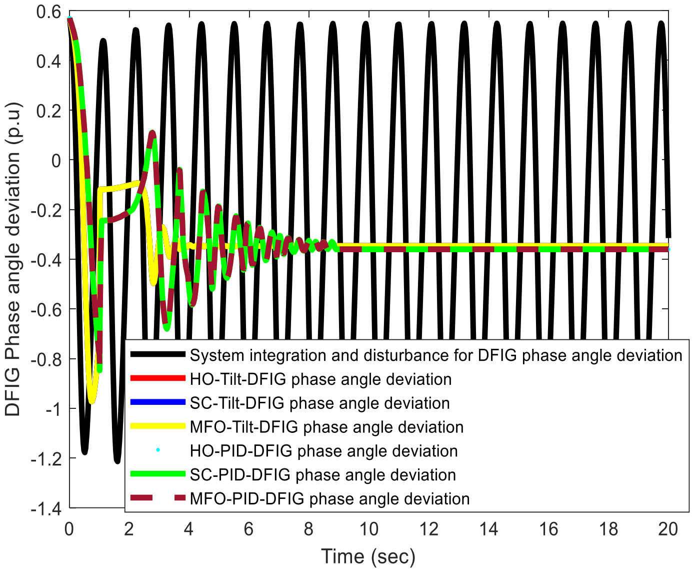

Figure 11. DFIG phase angle deviation

Variations in DFIG phase angle deviations for the Tilt and PID controllers were presented, and Table 2 shows numerical transient analysis results for OS, US, and ST, which are crucial indicators of each algorithm's success. The performances of the Tilt controller-based HO, MFO, and SC algorithms were better than those of the PID controller-based HO, MFO, and SC algorithms.

Table 2. Improved OS, US and ST damping oscillation for DFIG phase angle deviation

Optimization Techniques	OS	US	ST	Optimization Techniques	OS	US	ST
HO-Tilt	-0.095198	-0.96989	4.02017	HO-PID	0.108861	-0.83953	8.95122
SC-Tilt	-0.095198	-0.96989	4.02017	SC-PID	0.108861	-0.83953	8.95122
MFO-Tilt	-0.095198	-0.96989	4.02017	MFO-PID	0.108861	-0.83953	8.95122
Integrated	0.54741	-1.2694	-	Integrated	0.54741	-1.2694	-

Before the improved OS, the US and ST damping oscillation for DFIG phase angle deviation, the system is unstable during the simulation period without a controller, and its ST is not taken into consideration. as illustrated in Figure 11. ST is the time it takes each algorithm applied in the controller's design to stabilize and control.

3.3. Output voltage variation characterization of algorithm robustness

Figure 12 presents the output-voltage oscillation and robustness of the HO, SC, and MFO controllers, based on their performance; the operating conditions were unchanged. The oscillation demonstrations improved significantly in terms of output-voltage deviations for the Tilt and PID controllers.

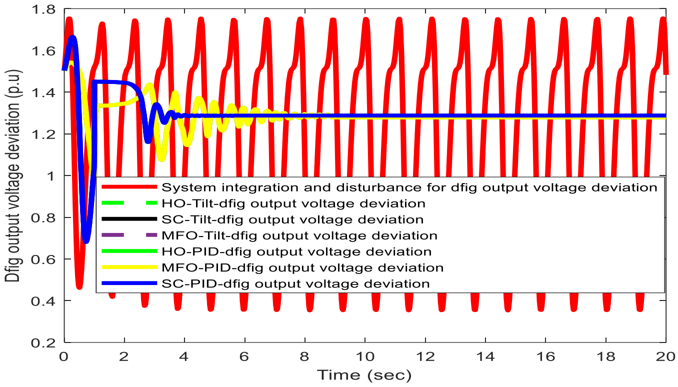

Figure 12. DFIG output voltage deviation

The figure shows a numerical momentary study, in terms of OS, US, and ST, which are essential indicators of the effectiveness of each algorithm, and the robustness of Tilt controllers based on MFO, HO, and SC algorithms, which are slightly better than the PID controller based on MFO and HO.

Table 3. Improved OS, US and ST damping oscillation for DFIG output voltage deviation

Optimization Techniques	OS	US	ST	Optimization Techniques	OS	US	ST
HO-Tilt	1.665	0.693	3.949	HO-PID	1.541	0.933	9.079
SC-Tilt	1.665	0.693	3.949	SC-PID	1.665	0.693	3.949
MFO-Tilt	1.665	0.693	3.949	MFO-PID	1.541	0.933	9.079
Integrated	1.750	0.346	-	Integrated	1.750	0.346	-

Table 3 presents numerical damping oscillation for the DFIG output voltage deviation for the three compared algorithms, HO, SC, and MFO, which show robustness improvements in terms of OS, US, and ST variations damping for the Tilt and PID controllers. Performances of Tilt and PID controllers based on SC algorithms were more pronounced than those of controller-based HO and MFO algorithms, as indicated by ST in Table 3.

4. CONCLUSIONS

An integrated Kundur's two-area network DFIG Damping, controller oscillations were demonstrated, an optimal wind rotor power coefficient (C_p) has been examined at 0.48, very close to the theoretical Benz limit, output voltage and phase angle oscillations deviations were presented. The controllers' performances were compared with three techniques: Tilt controllers based on MFO, HO, and SC algorithms. The performances of the MFO, HO, and SC algorithms are slightly better than those of the PID controller-based. In the future, damping controllers such as flexible alternating current transmission systems (FACTS) with power oscillation dampers (POD) can be introduced into the system.

REFERENCES

[1] S. Rajendran et al., “Wind Turbine Emulators—A Review,” *Processes*, vol. 11, p. 747, 2023. https://doi.org/10.3390/pr11030747.

[2] B. Dasu, M. Sivakumar, and R. Srinivasarao, “Interconnected multi-machine power system stabilizer design using whale optimization algorithm,” *Prot. Control Mod. Power Syst.*, vol. 4, no. 2, pp. 1–11, 2019. https://doi.org/10.1186/s41601-019-0116-6.

[3] J. X. Jin, R. H. Yang, R. T. Zhang, Y. J. Fan, Q. Xie, and X. Y. Chen, “Combined low voltage ride through and power smoothing control for DFIG/PMSG hybrid wind energy conversion system employing a SMES-based AC-DC unified power quality conditioner,” *Int. J. Electr. Power Energy Syst.*, vol. 128, p. 106733, 2021. https://doi.org/10.1016/j.ijepes.2020.106733.

[4] A, Sabo, B.Y, Kolapo, T.E, Odoh, M., Dyari, N.I, Abdul Wahab, V. Veerasamy, “Solar, Wind and Their Hybridization Integration for Multi-Machine Power System Oscillation Controllers Optimization: A Review,” *Energies,* vol. 16, no. 24, 2023. https://doi.org/10.3390/en16010024.

[5] N. K. Kumar et al., “Fuzzy Logic-Based Load Frequency Control in an Island Hybrid Power System Model Using Artificial Bee Colony Optimization,” *Energies*, vol. 15, no. 6, p. 2199, 2022. https://doi.org/10.3390/en15062199.

[6] A. Sabo et al., “A review on techniques used for solving the economic load dispatch problems: categorization, advantages, and limitations,” *Vokasi UNESA Bulletin of Engineering, Technology and Applied Science*, vol. 2, no. 1, pp. 36–47, 2025. https://doi.org/10.26740/vubeta.v2i1.35591.

[7] G. Shahgholian and A. Fathollahi, “Analyzing Small-Signal Stability in a Multi-Source Single-Area Power System with a Load-Frequency Controller Coordinated with a Photovoltaic System,” *AppliedMath*, vol. 4, no. 2, pp. 452–467, 2024. https://doi.org/10.3390/appliedmath4020024.

[8] M Rawal; D.C Nauityal; M.S Rawat, “Analysis of small signal stability in DFIG integrated power system,” *Proceedings of the 2021 International Conference on Advances in Electrical, Computing, Communication and Sustainable Technologies (ICAECT*), Bhilai, India, 2021. https://doi.org/10.1109/ICAECT49130.2021.9392505.

[9] A. Sabo et al., “Modified Multimachine Power System Design with DFIG-WECS and Damping Controller,” *Energies*, vol. 17, p. 1841, 2024. https://doi.org/10.3390/en17081841.

[10] A. Benmessaoud Gabis, Y. Meraihi, S. Mirjalili, A. Ramdane-Cherif, and The Author(s), “A comprehensive survey of sine cosine algorithm: variants and applications,” 2021. https://doi.org/10.1007/s10462-021-10026-y.

[11] A. Sabo; T.E Odoh; H. Shahinzadeh; Z. Azimi; M. Moazzami. “Implementing Optimization Techniques in PSS Design for Multi-Machine Smart Power Systems: A Comparative Study,” *Energies,* vol. 16, 2465, 2023. https://doi.org/10.3390/en16052465.

[12] M. H. Amiri *et al.*, “Hippopotamus optimization algorithm: a novel nature-inspired optimization algorithm,” *Scientific Reports*, vol. 14, p. 5032, 2024. https://doi.org/10.1038/s41598-024-54910-3.

[13] L. Kunjumuhammed; S. Kuenzel; B.C Pal. “Simulation of Power System with Renewables,” *AcademicPress: Cambridge, MA, USA*,2019; ISBN 0128112549.

[14] L. Kunjumuhammed., S. Kuenzel., and P. C. Bikash, “Simulation of power system with renewables,” *United Kingdom*, *Academic Press.* pp. 1-180, 2019. https://doi.org/10.1016/B978-0-12-811187-1.00001-9.